Highlights from the Pierre Auger Observatory

Michael Unger[*a] **for the Pierre Auger Collaboration**[b]

[a]*Karlsruhe Institute of Technology, Institut für Kernphysik, Karlsruhe, Germany*
[b]*Observatorio Pierre Auger, Av. San Martín Norte 304, 5613 Malargüe, Argentina*
E-mail: auger_spokespersons@fnal.gov
Full author list: http://www.auger.org/archive/authors_icrc_2017.html

In this contribution we summarize the highlights from the Pierre Auger Observatory presented at the 35th International Cosmic Ray Conference. We discuss the update of the measurement of the energy spectrum of cosmic rays over a wide range of energies ($10^{17.5}$ to above 10^{20} eV), studies of the cosmic-ray mass composition with the fluorescence and surface detector of the Observatory, the discovery of a large-scale anisotropy in the arrival direction of cosmic rays above 8×10^{18} eV and indications of anisotropy at intermediate angular scales above 4×10^{19} eV. Moreover, we report on tests of hadronic interactions beyond LHC energies, multi-messenger analyses with neutral primaries and the progress of the upgrade of the Observatory, AugerPrime, aimed at elucidating the origin of the observed flux suppression at ultra-high energies.
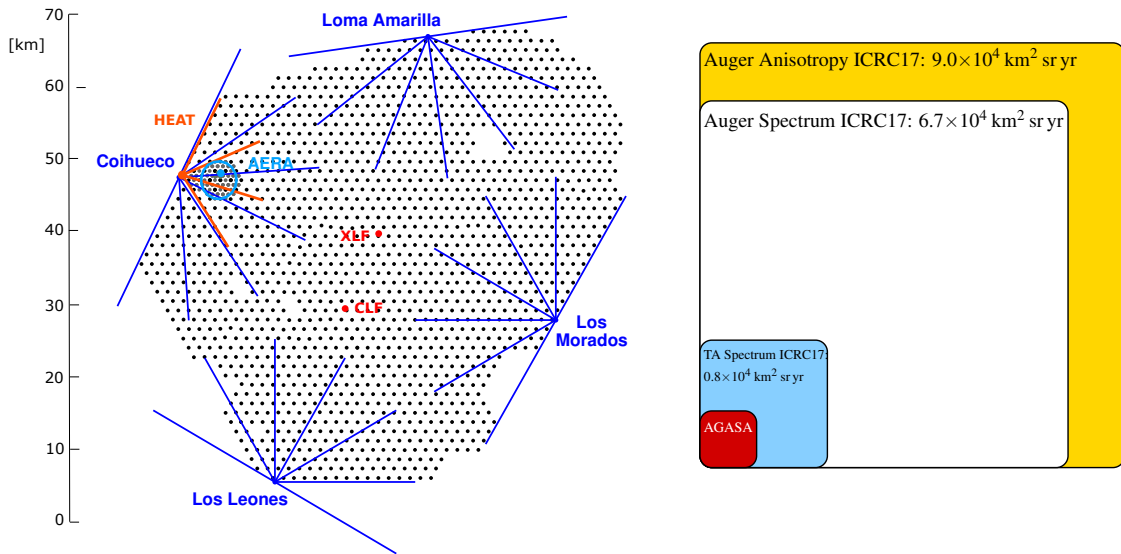
35th International Cosmic Ray Conference — ICRC2017
*10–20 July, 2017*
Bexco, Busan, Korea

---

[*]Speaker.

Figure 1: *Left:* Layout of the Pierre Auger Observatory. Water-Cherenkov detectors are shown as black dots and the azimuthal field of views of the 27 fluorescence telescopes is indicated by blue and red lines. The location of the two laser facilities (CLF and XLF) for the monitoring of the aerosol content in the atmosphere are shown with red dots and the area equipped with radio antennas (AERA) is marked with a light-blue circle. *Right:* Illustration of the exposures available for two of the Auger analyses described in this paper (yellow and white) and the exposures collected by the Telescope Array (blue) and AGASA (red).

1. Introduction

In this article we summarize highlights from the presentations of the Pierre Auger Coll. at the 35th International Cosmic Ray Conference [1, 2]. The Pierre Auger Observatory [3] is the largest facility built so far to detect cosmic rays. It is located in the province of Mendoza, Argentina and has been in operation since 2004. Cosmic rays are studied by combining a Surface Detector (SD) and a Fluorescence Detector (FD) to measure extensive air showers. The SD consists of 1600 water-Cherenkov detectors on a 1500 m triangular grid (SD 1500) over an area of $\sim$3000 km^2, and of an additional 61 detectors covering 23.5 km^2 on a 750 m grid (SD 750). The SD is overlooked by 27 fluorescence telescopes located in five buildings on its periphery. 24 telescopes cover 30° in azimuth and elevations from 1.5° to 30° above the horizon. Three additional telescopes enlarge the elevation coverage to 60° for low-energy showers. The SD is used to measure photons and charged particles at ground level with a duty cycle near 100% and the FD to observe the longitudinal development of air showers in the atmosphere during dark nights, and under favorable meteorological conditions with a duty cycle of about 13%. This setup is complemented by the Auger Engineering Radio Array (AERA) to study radio emission from air showers [4]. The layout of the Observatory is shown in the left panel of Fig. 1 and the exposure collected between January 2004 and December 2016 is illustrated in the right panel. The exposure thus far collected is close to 10^5 km^2 sr yr for studies of anisotropies in the arrival directions of cosmic rays. The large exposure and an 85% coverage of the celestial sphere are the prerequisites to perform the precise measurements of the flux, composition and anisotropy of ultra-high-energy cosmic rays (UHECRs) described in the following.
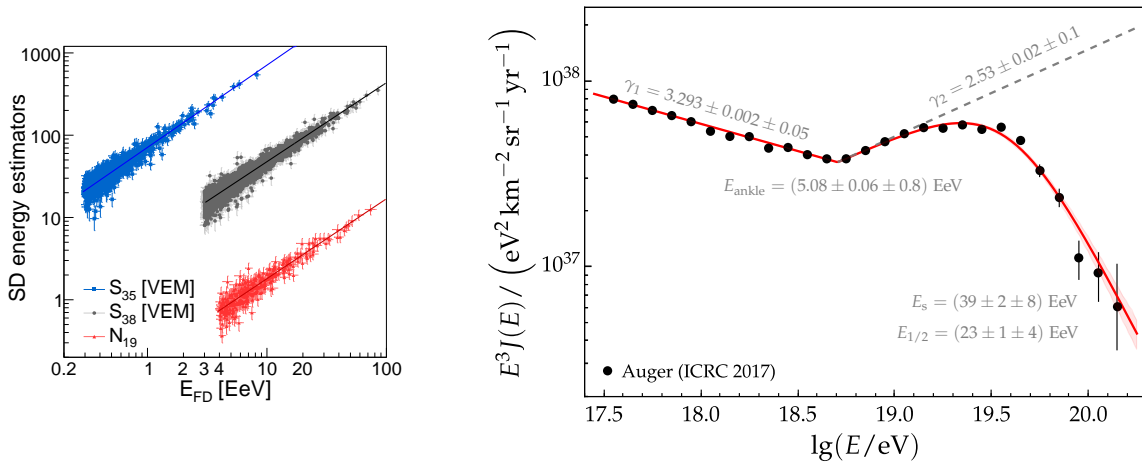
Figure 2: *Left*: Energy calibration of the surface detector. The shower size measured for near-vertical events with the SD 1500 (S_{38}) and SD 750 (S_{35}) array and for inclined showers (N_{19}) is shown as a function of the energy measured with the fluorescence telescopes (E_{FD}). *Right*: Combined energy spectrum. The red line shows a fit to the spectrum with a broken power law and a suppression at ultra-high energies. The gray dashed line indicates the same broken power law without suppression. The fitted spectral indices and energies of the break and suppression are superimposed together with their statistical and systematic uncertainties.

2. Energy Spectrum

We use four different data sets to derive the energy spectrum of cosmic rays [5]. The two "near-vertical" data samples consist of showers arriving at zenith angles $\leq 60°$ detected by the SD 1500 and SD 750 arrays with an energy threshold of 3×10^{18} eV and 3×10^{17} eV, respectively. "Inclined" showers with zenith angles between $60°$ and $80°$ are studied with the SD 1500 array above 4×10^{18} eV. Finally, the "hybrid" sample consists of events above 10^{18} eV detected by the FD simultaneously with at least one station of the SD. From each of the data sets an independent energy spectrum is derived and, after establishing the compatibility between the individual spectra, the four measurements are statistically combined to obtain our best estimate of the energy spectrum of cosmic rays above 3×10^{17} eV, from a total exposure of 6.7×10^4 km^2 sr yr, collected between January 2004 and December 2016.

The method to derive the spectra is entirely data-driven and free of model-dependent assumptions about hadronic interactions in air showers. For the surface detector data, we transform the measured shower sizes to a size estimator that is independent of zenith angle by using the method of constant intensities for the near-vertical data [6] and templates of the footprint of the particle densities at the ground for the inclined data set [7]. These attenuation-corrected shower sizes are used as energy estimates after calibrating them with the calorimetric energy available for events that have been observed simultaneously with the surface and fluorescence detectors, as shown in the left panel of Fig. 2.

The main ingredients for the energy scale of the Observatory are a precise laboratory measurement of the fluorescence yield [8], the optical calibration of the fluorescence telescopes [9] and the monitoring of the light attenuation in the atmosphere [10]. At this conference we presented improvements of the data-driven estimate of the "invisible energy" (i.e. the amount of energy in air showers carried away by muons and neutrinos), the event reconstruction at low energies, the

spectral calibration of the telescopes and the determination of the aerosol content of the atmosphere [5, 11, 12]. These improvements result in an update of the energy scale of the Observatory with changes of $\leq 4\%$. The overall systematic uncertainty of the energy scale remains at 14% [13]. An independent determination of the Auger energy scale using the radiation energy in the radio signal of air showers with AERA might be possible in the near future [14, 15].

The combined energy spectrum is shown in the right panel of Fig. 2. To quantify the features of the spectrum, we fitted the flux with a power law allowing for a break in the spectral index at E_{ankle} and a suppression of the flux at ultra-high energies $\propto \left(1 + (E/E_{\mathrm{s}})^{\Delta_{\mathrm{s}}}\right)^{-1}$. As can be seen, we find that the position of the "ankle" in the cosmic-ray spectrum is at $E_{\mathrm{ankle}} = (5.08 \pm 0.06(\mathrm{stat.}) \pm 0.8(\mathrm{syst.}))$ EeV where the spectral index hardens by $\Delta\gamma \sim -0.76$. A power-law extension of the flux above the ankle towards ultra-high energies is clearly excluded by our measurement and we find a suppression energy of $E_{\mathrm{s}} = (39 \pm 2(\mathrm{stat.}) \pm 8(\mathrm{syst.}))$ EeV and a softening of $\Delta_{\mathrm{s}} = (2.5 \pm 0.1(\mathrm{stat.}) \pm 0.4(\mathrm{syst.}))$. The current exposure allows us to probe the spectrum up to $10^{20.15}$ eV where we find that the flux is suppressed by more than an order of magnitude with respect to a power-law continuation. The energy at which the integral flux drops by a factor of two below what would be expected without suppression is found to be $E_{1/2} = (23 \pm 1(\mathrm{stat.}) \pm 4(\mathrm{syst.}))$ EeV. This value is at considerable odds with $E_{1/2} = 53$ EeV as predicted in [16] for the suppression of the flux of protons produced uniformly in extragalactic space suffering energy losses due to photo-pion production in interactions with the photons of the cosmic microwave background radiation during propagation to Earth.

3. Mass Composition

The mass composition of cosmic rays is studied by measuring the atmospheric depth, X_{max}, at which the number of particles in an air shower reaches its maximum. On average light primaries penetrate deeper into the atmosphere than heavy primaries ($\langle X_{\mathrm{max}}\rangle \propto \lg(E/A)$ where A is the nuclear mass number) and the position of shower maximum fluctuates more for light than heavy primaries. The measurement of the average shower maximum as a function of energy with the FD is shown as blue dots in the right panel of Fig. 3. This measurement is based on 42,466 events above $10^{17.2}$ eV, out of which 62 have been detected at the highest energy ($E > 10^{19.5}$ eV) [17]. Biases from detector effects, e.g. due to the limited acceptance of the fluorescence telescopes, are avoided using the analysis methods explained in [18]. We find that the $\langle X_{\mathrm{max}}\rangle$ evolves with energy at a rate of 79 g/cm^2/decade and 26 g/cm^2/decade with a break in the evolution at $10^{18.33\pm0.02}$ eV, i.e. about a factor 2.5 lower in energy than the break in flux reported in the previous section. Predictions of the energy evolution of $\langle X_{\mathrm{max}}\rangle$ from air shower simulations are around 60 g/cm^2/decade, irrespective of the mass of the primary and the model used to simulate hadronic interactions. It can therefore be concluded that the average mass of cosmic rays evolves towards a lighter composition between $10^{17.2}$ and $10^{18.33}$ eV, qualitatively consistent with a transition from a heavy Galactic composition, to a light extragalactic composition. At higher energies the trend is reversed and the average mass increases with energy.

The statistics collected with the relatively low duty cycle of FD do not yet allow us to study the composition at energies where the flux suppression is observed. At these energies we rely instead on measurements with the SD. However, previous measurements from Auger have shown that air

4
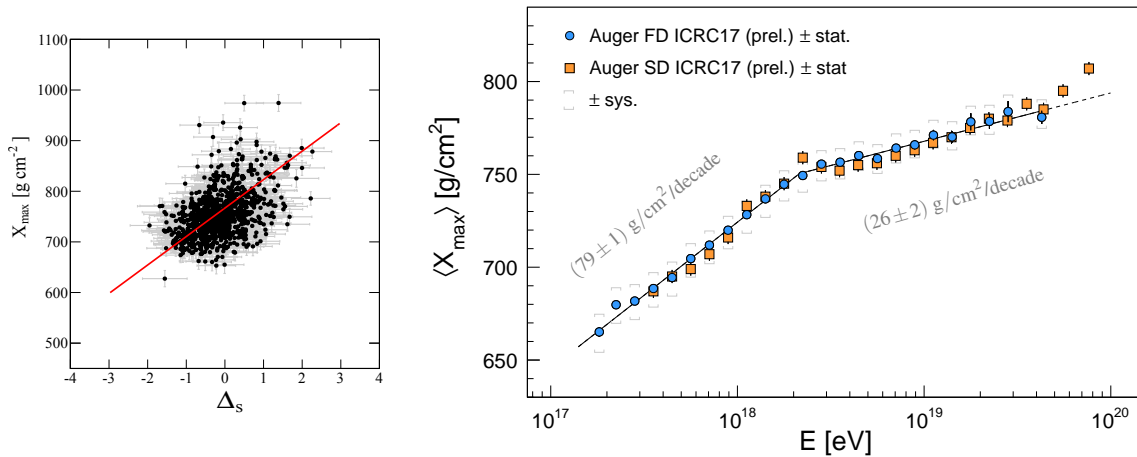
Figure 3: *Left*: Calibration of the SD variable Δ_S with X_{max} measured with the FD. *Right*: Average shower maximum, $\langle X_{max} \rangle$, from FD (blue dots) and SD (orange squares). A fit of the FD measurements with a broken linear function in $\lg(E)$ is displayed as a solid black line. Its extrapolation to high energies is indicated with a dashed line. The values of the fitted elongation rates are shown in gray.

shower simulations fail to reproduce salient features of the SD data [19–21]. We therefore follow a similar approach as for the energy spectrum and calibrate the mass observable from the SD with X_{max} from the FD.

Here we present results using the time profiles of the signals recorded with the SD stations, employing the fact that the *risetime* [22] of these signals depends on the distance of the shower maximum to the ground and the relative amount of muons and electrons detected. For each event, we construct the risetime-related variable Δ_S [23] and correlate it with X_{max} from the FD as displayed in the left panel of Fig. 3. After the calibration function that relates Δ_S to X_{max} is determined separately for the SD 1500 and SD 750 arrays, the energy evolution of $\langle X_{max} \rangle$ can be measured with the surface detector over a wide range of energies. The comparison of $\langle X_{max} \rangle$ from the FD and SD is shown in the right panel of Fig. 3. As can be seen, the two measurements are in good agreement, as is to be expected due to the cross-calibration. At ultra-high energies the superior statistics of the SD (517 events above $E > 10^{19.5}$ eV) give two data points more than obtained with the FD. Interestingly, these two last bins above $10^{19.6}$ eV do not follow the evolution of the composition seen at lower energies. This might be an indication that the increase of the average nuclear mass with energy is slowing at the highest energies. However, the final point is just $\sim 3\sigma$ above the low-energy extrapolation of the $\langle X_{max} \rangle$ from SD and therefore more data are needed to study this energy region.

Additional information on the composition can be obtained at the expense of an increased model dependence by comparing the measured $\langle X_{max} \rangle$ values directly to predictions of air shower simulations. This is shown in the left panel of Fig. 4, where it can be seen that around the break of $\langle X_{max} \rangle$ at $10^{18.3}$ eV, the composition is very light (even compatible with a pure proton composition for shower simulations with the QGSJ𝚎𝚝II hadronic interaction model) and the average mass increases to a value between proton and iron at the highest energies, with the exact relative position depending on the model. Note that the three hadronic interaction models used for the simulations shown in Fig. 4 have all been tuned to match data from the LHC [24–26]. Older versions of these
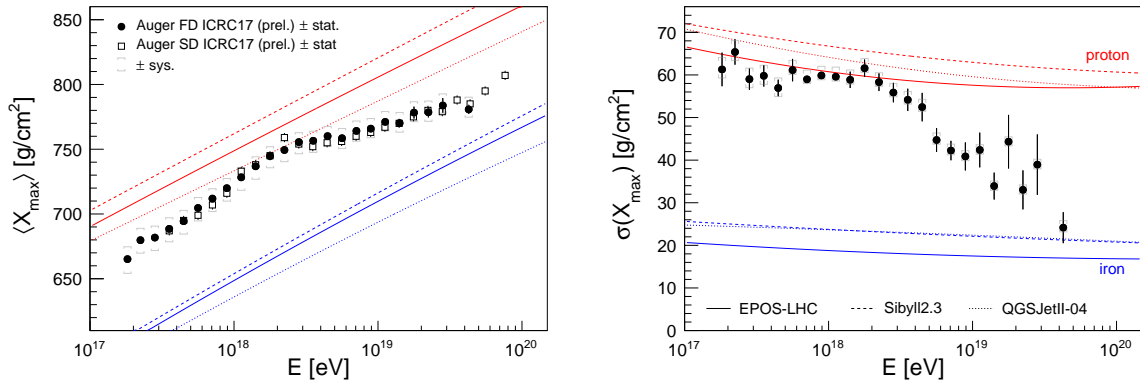
Figure 4: Comparison of $\langle X_{\max} \rangle$ (left) and $\sigma(X_{\max})$ (right) to predictions from simulations of proton- and iron-induced air showers.

models are at odds with laboratory measurements at equivalent fixed-target beam energies of up to 10^{17} eV, and can therefore not be used to reliably interpret the data.

In addition to the average of $X_{\max}$, its standard deviation, $\sigma(X_{\max})$, can also be determined from the data of the FD and the results are shown in the right panel of Fig. 4. A large value of $\sigma(X_{\max})$ can originate from either a light composition or a mixed composition, where in the latter case the difference in $\langle X_{\max} \rangle$ of different nuclei adds to the overall width of the $X_{\max}$ distribution. The data at low energies is compatible with both possibilities. At high energies, $\sigma(X_{\max})$ decreases indicating a rather pure and heavy composition. It was shown at this conference [17] that using the approach of [27] one can find compositions that result in values of $\langle X_{\max} \rangle$ and $\sigma(X_{\max})$ that are compatible with the Auger data if hadronic interactions in air showers are similar to the ones predicted by EPOSLHC or SIBYLL2.3. However, for simulations with QGSJETII-04, the derived average mass is too light to produce shower fluctuations as narrow as the measured ones and this model is at odds with our data.

An interpretation of the full $X_{\max}$ distribution in each energy bin is achieved by fitting a superposition of $X_{\max}$-templates obtained from simulations of p-, He-, N- and Fe-induced air showers to the data. At this conference we presented an update of our previous study [28] with increased statistics at high energies and for the first time also for data below $10^{17.8}$ eV. The resulting mass fractions are shown in Fig. 5. At high energies they are compatible with our earlier finding that the composition is dominated by a single elemental group starting from protons below the ankle and going through helium to nitrogen as the energy increases. Depending on the hadronic interaction model, a small proton fraction may persist up to ultra-high energies and there might be an iron contribution emerging above $10^{19.4}$ eV. The aforementioned difficulty of describing $\langle X_{\max} \rangle$ and $\sigma(X_{\max})$ with QGSJETII-04 is also visible in the lower panel of Fig. 5, where the probability of the fits is shown. The fit probabilities obtained with QGSJETII-04 are consistently low at around 0.01 above $10^{17.8}$ eV. Therefore, the mass fractions obtained with QGSJETII-04 should be interpreted with care.

At the lowest energies, we find hints for a contribution from iron primaries that disappears rapidly with increasing energy. The proton fraction between $10^{17.2}$ and $10^{17.7}$ eV is found to be approximately constant at a value of 38%, 28% and 25% for EPOSLHC, SIBYLL2.3 and QGSJETII-04 respectively. These estimates of the proton fraction are based on 7498 events and have a sta-
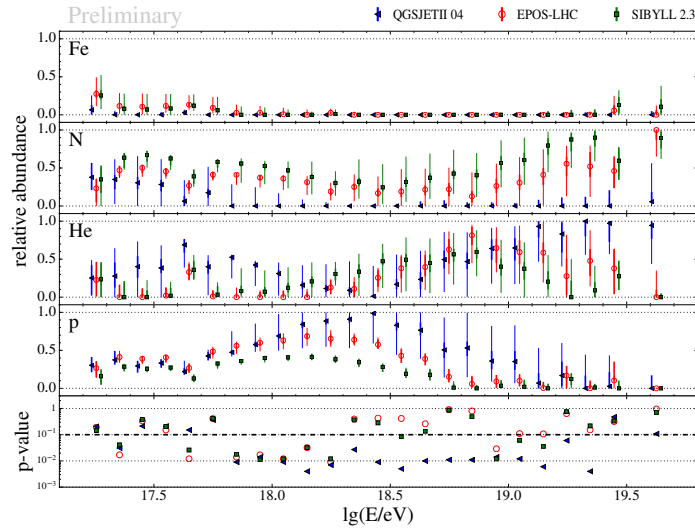
Figure 5: Results from a fit of the $X_{\max}$ distributions with a superposition of p-, He-, N- and Fe-induced air showers. The upper four panels show the best-fit mass fractions and the goodness of fit is displayed in the lowest panel. Thick error bars denote the statistical uncertainties, thin error bars the systematic ones.

tistical and systematic uncertainty of 2% and $\leq 9\%$ respectively. For comparison, a recent attempt to estimate the light-mass fraction from $X_{\max}$ was based on 118 events only [29]. The mass fractions presented here complement the findings of the KASCADE-Grande Coll. which reported a "knee" in the flux of the iron component at $10^{16.9}$ eV and an "ankle" of the light component at $10^{17.1}$ eV [30, 31]. It can be concluded that the new results from the Pierre Auger Observatory on the mass composition at low energies give important experimental constraints to the modeling of a possible transition from a heavy Galactic to a light extragalactic cosmic-ray component between 10^{17} and 10^{18} eV.

We end this section with the usual caveats about the model dependence of the interpretation of air-shower observables in terms of mass. The mass fractions derived from the $X_{\max}$ distribution are very sensitive to details of the modeling of hadronic interactions in air showers and the differences between mass fraction derived using the three "post-LHC" models do not necessarily bracket the actual uncertainty on the fractions. However, barring an onset of new physics in hadronic interactions at $10^{18.3}$ eV, the energy evolution of $\langle X_{\max} \rangle$ and $\sigma(X_{\max})$ are robust indicators of a gradual increase of the average nuclear mass of cosmic rays with energy. Further model-independent evidence for a mixed mass composition around the ankle was found in a study of correlations between $X_{\max}$ and the shower size measured with the SD [32].

4. Interpretation of Mass Composition and Spectrum

For a possible astrophysical interpretation of our results on the mass composition and energy spectrum, we considered a scenario in which the sources of UHECRs are of extragalactic origin and accelerate nuclei in electromagnetic processes with a rigidity-dependent maximum energy, $E_{\max}(Z) = E_{\max}(\text{p})/Z$, where Z denotes the charge and $E_{\max}(\text{p})$ is the maximum energy for protons. In a previous study [33] we reported that within this scenario a good description of the shape of
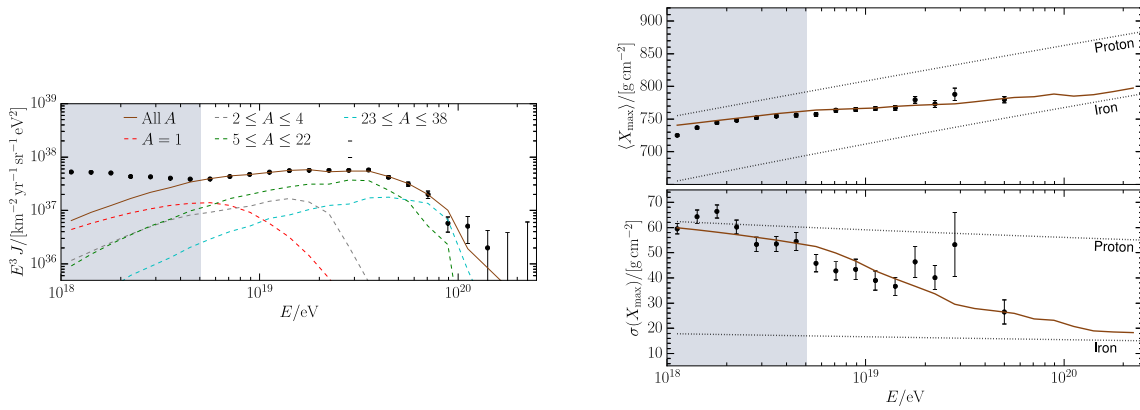
Figure 6: Mixed composition scenario including the effects of a discrete source distribution and the propagation of cosmic rays through the extragalactic photon and magnetic fields compared to the energy spectrum (left) and $\langle X_{max} \rangle$ and $\sigma(X_{max})$ (right). The fit was performed in the energy range above the shaded region and the data points are measurements from the Pierre Auger Observatory presented at the previous ICRC [18,40].

the measured energy spectrum as well as the energy evolution of the X_{max} distributions can be achieved if the sources accelerate a primary nuclear mix consisting of p, He, N and Si, if the primary spectrum follows a power law $\propto E^{-\gamma}$ with a spectral index $\gamma \sim 1$ and if the maximum energy of protons is about $10^{18.7}$ eV. In this case, the observed increase in the average nuclear mass is explained by the disappearance of light nuclei from the overall composition mix as the energy increases and the flux suppression is caused by both, energy losses during extragalactic propagation and maximum energy, of the highest-charge nucleus.

At this conference we presented further investigations of this astrophysical scenario [34]. The homogeneous distribution of sources assumed in our previous calculations was replaced by discrete sources distributed according to the model of the local large-scale structure from [35] and with a source density of $10^{-4}/\text{Mpc}^3$. Furthermore, we studied the effects of the extragalactic magnetic field (EGMF) on the inferred source parameters by tracking the cosmic-ray trajectories through the EGMF model of [36] during the propagation from the sources to Earth.

A fit of the data with this extended model is shown in Fig. 6. It provides a good overall description of the data and the goodness of fit is similar to the one achieved with the simpler model used in our previous study. The energy range below the ankle is excluded from the fit (as indicated by the shaded region) to avoid the modeling of possible contributions of Galactic cosmic rays and/or protons originating from photo-nuclear interactions in the source environment [37,38]. Comparing the best-fit parameters of the extended model with our previous results, we found that the details of the local large-scale structure of matter are of minor importance for the derived parameters of the source spectra. But by including in the calculation the diffusion in the EGMF, we derive a spectral index of $\gamma \sim 1.6$, i.e. significantly softer than $\gamma \sim 1$ as obtained without magnetic fields. This softening is caused by the suppression of the cosmic ray flux at low rigidities when the time it takes cosmic rays to diffuse to Earth is comparable to the age of the universe [39]. Therefore the presence of magnetic fields in the intergalactic space needs to be taken into account when interpreting cosmic ray data, especially when the field strength is relatively strong as assumed in this study.

8
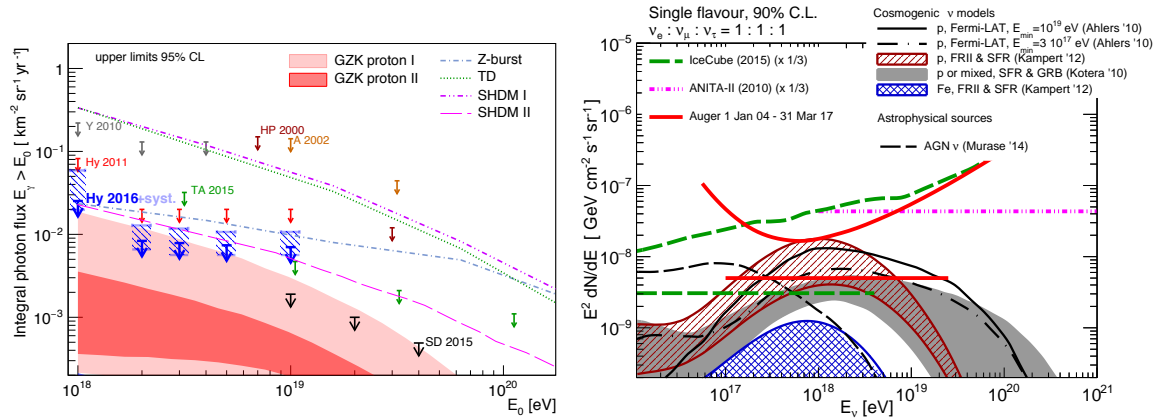
Figure 7: Upper limits on the diffuse photon (left) and neutrino flux (right) compared to limits from other experiments and model predictions (see [41, 42] for references).

5. Searches for Neutrinos and Photons

Neutrinos and photons are ideal astrophysical messengers for targeted source studies, since they are not deflected in the Galactic and extragalactic magnetic fields. In addition, the diffuse flux of neutrinos and photons carries information about the propagation of cosmic rays, their mass and the spacial distribution of the cosmic-ray sources, These "cosmogenic" neutrinos and photons originate from pions produced in proton-photon interactions with intergalactic radiation fields and their subsequent decays. A further source of cosmogenic neutrinos is the beta decay of neutrons produced in the photo-nuclear interactions of cosmic-ray nuclei during propagation.

The identification of photons with the Pierre Auger Observatory relies on the fact that photon-induced air showers penetrate deeper in the atmosphere and produce fewer muons than showers initiated by protons or nuclei. The best separation power between photons and charged cosmic rays is achieved by hybrid observations of air showers in which both the longitudinal development and the particle densities at the ground are measured [41].

Neutrino-induced air showers are searched for by scanning the data for upward-going, near-horizontal events (Earth-skimming neutrinos) or down-going, near-horizontal events with a large electromagnetic component, i.e. a first interaction point that is very deep the atmosphere [42].

The targeted search for photon point-sources presented at this conference yielded no evidence for EeV photon emitters in any of the studied source classes [43]. No candidate for a neutrino-induced shower was found and we presented an update of our previous limit [44] on the neutrino flux from steady point-sources. The absence of neutrino events around the time of gravitational wave events produced by binary Black Hole (BH) mergers reported by the LIGO Collaboration [45] allowed us to constrain the amount of total energy emitted in EeV neutrinos by black hole mergers [46].

Results on the diffuse flux of high energy photons and neutrinos are shown in Fig. 7. As can be seen, our upper limits on the diffuse flux of photons are the most stringent limits to date and severely constrain "top-down" models in which it is assumed that UHECRs are the decay products of either super-heavy dark matter (SHDM), topological defects (TD) or Z^0 bosons created in interaction of extremely high energy neutrinos with the relic neutrino background (Z-burst). With our current

9
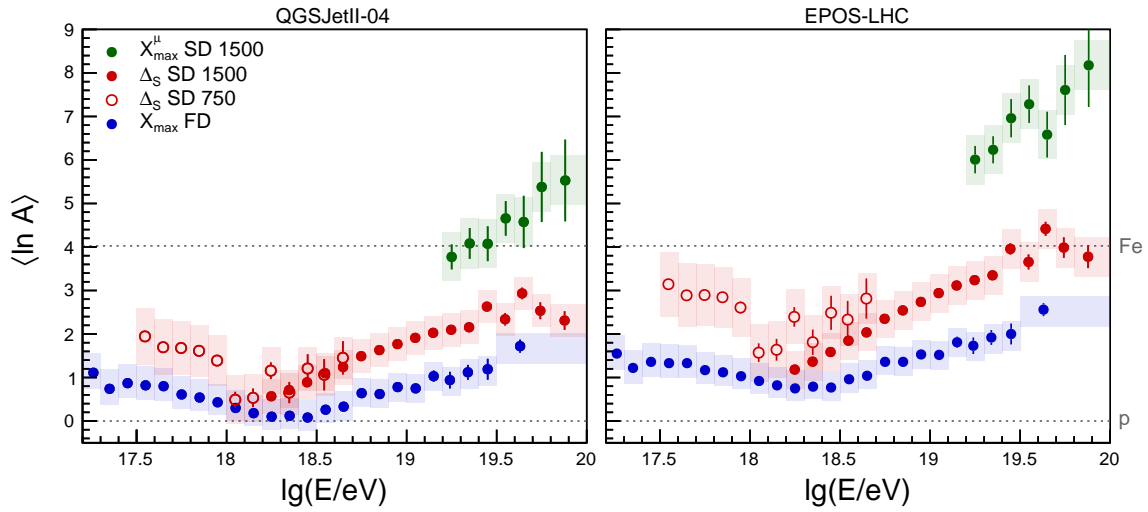
Figure 8: Average logarithmic mass, $\langle \ln A \rangle$, as a function of energy derived from the analyses presented at this conference: X_{max} (FD), Δ_S (SD) and X_{max}^{μ} (SD).

sensitivity we probe photon fractions of about 0.1% and can thus explore the region of photon fluxes predicted in some astrophysical scenarios for a proton-dominated mass composition. The updated limits on the diffuse neutrino-flux show that the sensitivity of the Pierre Auger Observatory to EeV neutrinos is comparable to that of dedicated neutrino experiments. Several predictions for cosmogenic neutrinos that arise in models explaining the origin of cosmic rays are excluded at 90% C.L., in particular those that assume proton primaries accelerated in sources with a strong redshift evolution.

6. Tests of Hadronic Interactions at Ultra-High Energies

Ultra-high energy air showers provide the opportunity to study hadronic interactions beyond energies accessible in the laboratory. In previous studies we reported the proton-air cross section at $\sqrt{s} = 57$ TeV [47], and a deficit in the predicted number of muons [20] and in the hadronic component [21] above $\sqrt{s} = 100$ TeV. Further inconsistencies in the modeling of hadronic interactions in air showers were revealed by studies of muon production depth [19] and the azimuthal asymmetry in the risetime of SD signals [48].

Whereas extrapolations of the $p + p$ cross sections measured at the LHC agree well with our measurement at high energies, it is more challenging to predict the muon content of air showers and thus the signals observed in the SD stations. The majority of muons in air showers are created in decays of charged pions when the energy of the pion is low enough such that its decay length is smaller than its interaction length. At ultra-high energies it takes several generations of interactions until the average pion energy is sufficiently small for pion decay to dominate. As a result, the total number of muons in an air shower depends on details of hadronic interactions along a chain of interactions. Hence, even small differences in the assumed properties of hadronic interactions can lead to a sizable effect on the predicted muon number when propagated over several generations of the particle cascade. In contrast, the longitudinal development, and in particular X_{max}, measured

by the FD is dominated by the first few interactions and is thus less susceptible to an accumulation of uncertainties of hadronic particle production over many generations.

The inconsistencies in the modeling of air showers can be quantified by converting the average properties of the ground signal measured with the SD to an average logarithmic mass, $\langle \ln A \rangle$, to provide a common scale between these different observables and the $X_{\max}$ measurements from the FD. This is shown in Fig. 8 for measurements presented at this conference. The average mass, derived from risetime-related variable Δ_S (obviously *without* the cross-calibration with FD described in Sec. 3) and from the update of the measurement of the average muon production depth [49], is compared to the $\langle \ln A \rangle$ estimated from $\langle X_{\max} \rangle$. As can be seen, neither of the two models can satisfactorily describe all three measurements at the same time and the models completely fail to describe the muon production depths, unless one considers the possibility of a trans-iron composition at ultra-high energies.

We conclude that even though recent hadronic interaction models were tuned to LHC data there is still ample room for further improvements. A revision of the models to bring the mass estimates from ground-level measurements in agreement to the ones from $X_{\max}$ will not only make the SD a more reliable tool for mass composition studies, but also improve the uncertainty of the modeling of $X_{\max}$ itself [50, 51].

7. Arrival Directions

At this conference the Pierre Auger Coll. announced the observation of a large-scale anisotropy in the arrival directions of cosmic rays above 8×10^{18} eV [52, 53]. Thanks to additional ~ 2.6 years of data and an optimized event selection, earlier hints [54] of a non-vanishing amplitude in the first harmonic in right ascension could be confirmed with a significance of 5.2σ.

Two energy bins, $4 \, \text{EeV} < E < 8 \, \text{EeV}$ and $E \geq 8 \, \text{EeV}$, were monitored since the start of data taking with the Observatory. The current measurements of the amplitude of the first harmonic in right ascension are $0.5^{+0.6}_{-0.2}\%$ and $4.7^{+0.9}_{-0.7}\%$, respectively. The events in the lower energy bin follow an arrival distribution consistent with isotropy, but in the higher energy bin a significant anisotropy was found, with a p-value of 2.6×10^{-8} under the isotropic null hypothesis. A skymap of the intensity of cosmic rays arriving above 8×10^{18} eV is shown in Fig. 9. The data can be well described by a dipole with a total amplitude of $6.5^{+1.3}_{-0.9}\%$. The reconstructed direction of the dipole points towards $(\ell, b) = (233°, -13°)$ and is indicated with a star in Fig. 9. This direction is about $125°$ from the Galactic Center, suggesting that the anisotropy has an extragalactic origin.

A potential cause for a dipole in the arrival directions of cosmic rays is the cosmological Compton-Getting effect [55], i.e. the anisotropy caused by the net motion of Earth with respect to the rest frame of UHECR sources. The predicted amplitude of the cosmological Compton-Getting effect is however only 0.6%, much smaller than the signal reported here.

Another possibility is that the dipole arises from spatial inhomogeneities in the distribution of sources or a dominant source whose image is blurred by the intergalactic and Galactic magnetic field. For instance, it is known that the distribution of nearby galaxies, as mapped by the 2MASS redshift survey (2MRS) [56], exhibits a dipolar structure [57]. If sources of UHECRs are a subset of these galaxies, then the arrival direction of cosmic rays at Earth should follow the same structure. The dipole of the flux-weighted distribution of infrared-detected galaxies in the 2MRS catalogue
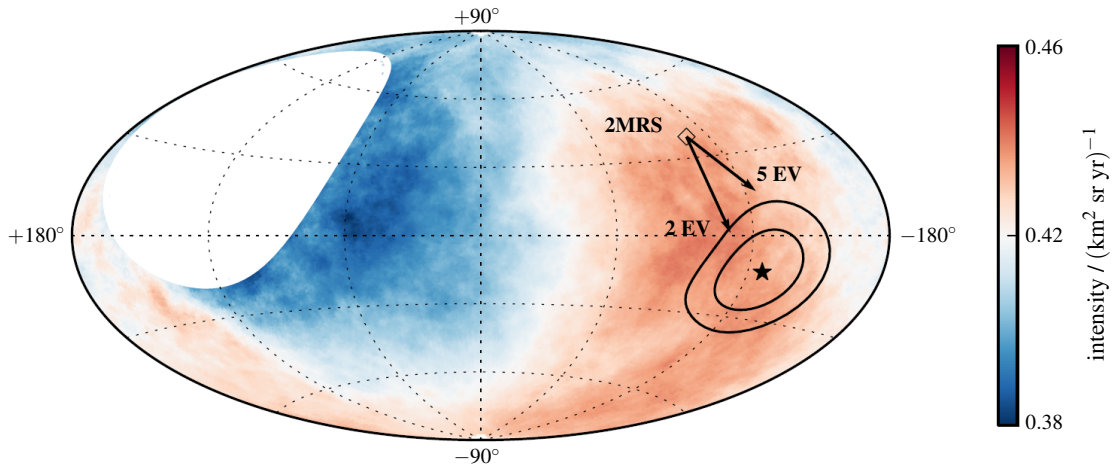
Figure 9: Map of the intensity in Galactic coordinates for $E \geq 8\,\text{EeV}$, smoothed by $45°$. The reconstructed dipole direction is indicated with a star, the contours represent the 68% and 95% CL regions. The direction of the dipole in the distribution of galaxies from 2MRS is shown by a diamond and the arrows indicate how this direction would be modified in a particular model of the Galactic magnetic field for two rigidities E/Z compatible with the composition shown in Fig. 5.

is shown as an open diamond in Fig. 9. It is $55°$ away from the central direction of the dipole discovered in the arrival direction of cosmic rays. To illustrate how the Galactic magnetic field could influence the observed direction of the 2MRS dipole, the deflected positions of this dipole, as predicted using a particular model of the Galactic magnetic field [58], are shown as arrows in Fig. 9 for two different cosmic-ray rigidities that are compatible with the composition fractions shown in Fig. 5. The agreement between the directions of the UHECR and 2MRS dipoles is improved by adopting these assumptions about the charge composition and the deflections in the Galactic magnetic field.

The origin of the discovered dipole remains at this point a subject of speculation. Additional studies of its properties will be performed soon, for instance the evolution of the dipole with energy and, with future data from AugerPrime, its dependence on rigidity. However, it can already be concluded that the direction of the anisotropy, pointing away from the Galactic center, provides strong support to the hypothesis of an extragalactic origin of the highest-energy cosmic rays.

Further studies of the arrival directions of UHECRs were performed at ultra-high energies and at intermediate angular scales [59]. We followed up the two searches with the largest deviations from isotropy from [60], now using an exposure of $9.0 \times 10^4\,\text{km}^2\,\text{sr yr}$, i.e. 35% more than in our previous study. We confirm the excess of events ("warm spot") above $5.8 \times 10^{19}\,\text{eV}$ in the direction of the Centaurus A radio galaxy within a search radius of $15°$ at a post-trial significance of $\sim 3.1\sigma$. Furthermore, an excess in the two-point correlation function between our data and the most luminous active galactic nuclei (AGNs), detected by *Swift*-BAT [61] ($D \leq 130\,\text{Mpc}$ and $L \geq 10^{44}\,\text{erg/s}$) above $6.2 \times 10^{19}\,\text{eV}$ within a search radius of $16°$, is found with a post-trial significance of $\sim 3.2\sigma$.

In a new study we investigated the compatibility of the detected arrival directions of UHECRs with flux models based on AGNs detected by *Fermi*-LAT (17 bright nearby AGNs from the 2FHL
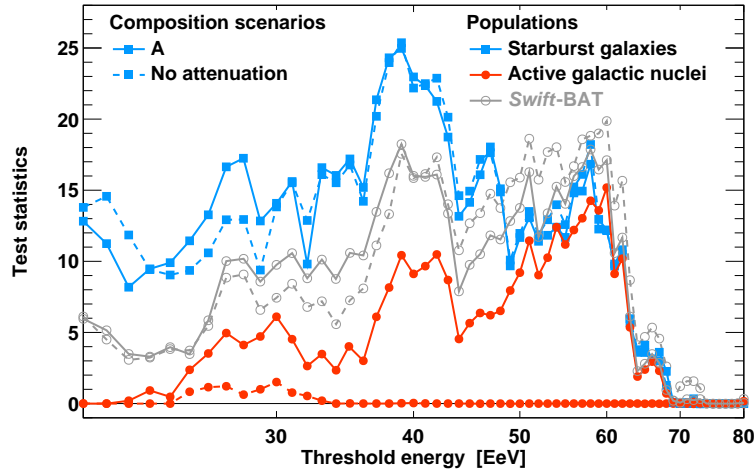
Figure 10: Test statistic as a function of the threshold energy for starburst galaxies (blue lines), gamma-ray AGNs (red lines) and *Swift*-BAT AGNs (gray lines). The continuous lines indicate the values of the test statistics obtained accounting for attenuation of the intensity due to energy losses, while the dotted lines refer to the values without any attenuation.

Catalog [62]) and 23 nearby starburst galaxies (SBGs) [63]. For the AGNs we assume that the UHECR intensity is proportional to the integral gamma-ray flux between 50 GeV and 2 TeV and for the SBGs we used the 1.4 GHz radio flux as an UHECR proxy noting that for SBGs detected in gamma rays the radio flux scales linearly with their gamma-ray luminosity [64]. The attenuation of the intensity due to energy losses en route to Earth is taken into account assuming different composition scenarios fitting our data [34]. The free parameters of this study are the smearing angle and the fraction of anisotropic cosmic rays originating from the intensity model. A cut on the threshold energy is optimized to maximize the signal and the optimization is penalized for through Monte-Carlo studies. The evolution of the test statistic (the likelihood ratio between isotropy and model for the best-fit isotropic fraction and smearing angle) as a function of threshold energy is shown in Fig. 10. As can be seen, the test statistics is maximized at 60 and 39 EeV for the AGN and SBG scenario, respectively. The smearing angle and the anisotropic fraction corresponding at maximum test statistic are 13° and 10% for the starburst-galaxies and 7° and 7% for the gamma-ray AGNs. Comparisons of the skymaps of the smeared data and SBG/AGN models are shown in Fig. 11. The post-trial significance is 2.7σ for the gamma-ray AGNs, while for the starburst galaxies we found a deviation from isotropy at the 4σ level.

It is worthwhile noting that all the searches presented here are *a posteriori* explorations. Numerous studies have been performed in the past with Auger data within and outside the collaboration. This makes it difficult to evaluate a proper penalty factor for all the previous searches. It is however noteworthy that all three "AGN-type" models (Centaurus-A only, *Swift*-BAT, 2FHL) yield a post-trial significance at the 3σ level, mainly driven by the "warm spot" in the direction of Centaurus-A. The same over-density of events contributes to the significance of the SBG model, but with a different interpretation as being caused by the bright starburst galaxies NGC 4945 and M83. In addition, the SBG model is able to describe the mild over-density of events observed around the South Galactic pole via contributions from NGC 1068 and NGC 253. With a post-trial significance at the 4σ level, the SBG model gives so far the strongest indication for an anisotropy
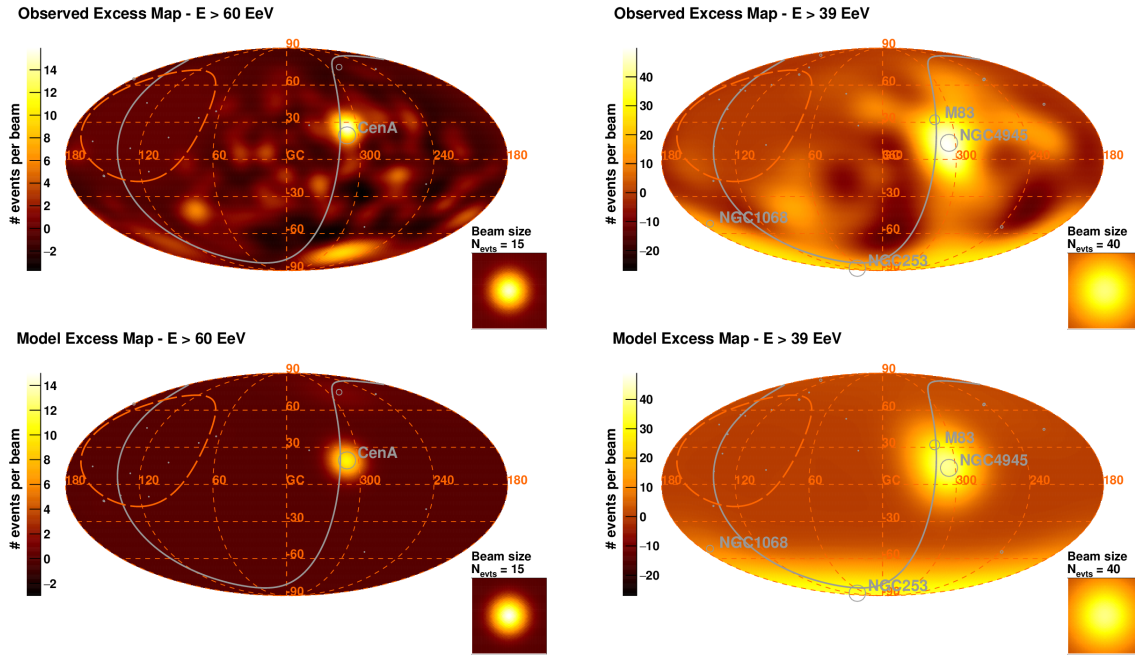
Figure 11: Skymaps of the observed (top) and model (bottom) event excess with respect to an isotropic background obtained with the best-fit parameters for the gamma-ray AGNs (left) and for the starburst galaxies (right) in galactic coordinates. The supergalactic plane is indicated as a gray line and the limit of the field of view of the Observatory is shown as a dashed red line. The signal for a particular number of events and the respective smearing angle is shown in the insets labeled as "beam size".

in the arrival directions of UHECRs at intermediate angular scales found in our data set. Of course correlation does not imply causation and therefore caution is required in identifying the sources of UHECRs prior to testing different catalogues and source weights, and a better understanding of the impact of magnetic deflections in the Galaxy on the intensity maps of the models.

8. Outlook: AugerPrime

The main results derived from the data collected with the Pierre Auger Observatory so far can be summarized as follows: The energy spectrum of UHECRs shows a pronounced break at around 5 EeV (the ankle) and a flux suppression at around 40 EeV. Above $10^{17.2}$ eV the average mass decreases, reaching a light composition at $10^{18.3}$ eV and increases again towards ultra-high energies with a possible hint of a change in the mass evolution above $10^{19.5}$ eV. Our non-detection of neutrinos and photons severely constrains top-down models and limits the redshift evolution allowed for proton accelerators. We measured the proton-air cross section at $\sqrt{s} = 57$ TeV and found it in good agreement with extrapolations from LHC energies, but our SD data reveals insufficiencies in the modeling of the hadronic component of air showers. On large angular scales the sky is anisotropic with a dipolar amplitude of about 7% at 8×10^{18} eV and there are indications for anisotropies at intermediate angular scales at ultra-high energies. These are obviously dramatic advancements of our understanding of UHECRs, but many open questions still remain. The Accordingly the Pierre
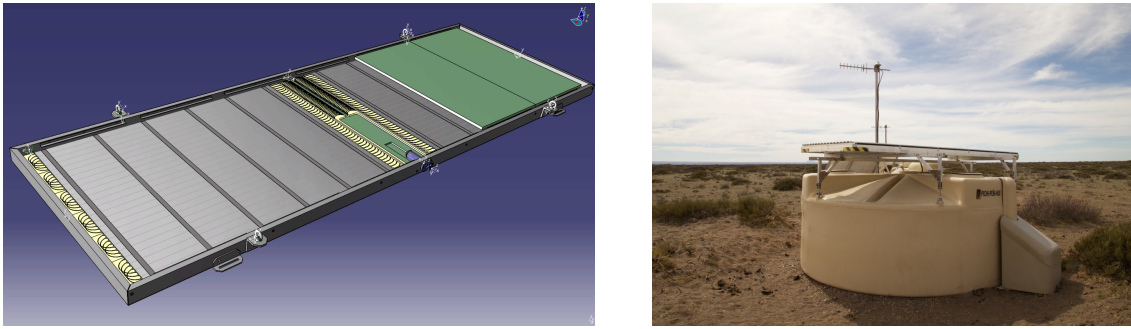
Figure 12: *Left:* Layout of the Surface Scintillator Detector (SSD); *Right:* One station of the AugerPrime Engineering Array.

Auger Coll. is currently upgrading the Observatory to address the following important problems:

Origin of the flux suppression: Is the flux suppression caused by energy losses of cosmic rays during the propagation from their sources to Earth or by the maximum energy of the astrophysical accelerators? Or maybe a combination of both?

Prospects for particle astronomy: What is the fraction of light elements at ultra-high energies? Is it large enough to perform charged particle astronomy with tolerable distortions from Galactic and extragalactic magnetic fields? How do the anisotropies reported in Sec. 7 depend on the particle rigidity?

Fundamental physics at ultra-high energies: Are the inconsistencies between air shower simulations and the surface detector data due to fundamental shortcomings in our understanding of hadronic multiparticle production? Can we constrain new physics phenomena, such as Lorentz invariance violation or extra dimensions at energies beyond those accessible at human-made accelerators?

The main focus of the upgrade of the Observatory, named "AugerPrime", is to provide a high-statistics sample of events with mass information at ultra-high energies which will be achieved by increasing the amount of information extracted from air shower with the SD [65, 66]. Each of the surface detector stations will be equipped with an additional 4 m^2 Surface Scintillator Detector (SSDs) installed on top of the existing Water-Cherenkov Detectors (WCDs) [69]. The layout of the upgraded surface detector stations is shown in Fig. 12. The WCD and SSD have a different response to the electromagnetic and muonic component of an air shower, and therefore the combined measurement allows to disentangle these two components and to provide an estimate of both, mass and energy of the shower, on an event-by-event basis. The detectors will be read out by new electronics with a faster and more accurate sampling of the signal [67]. Together with an extra small photomultiplier installed in each WCD the current dynamic range will be extended to more than 32 times the largest signals currently measured [68]. This setup is complemented by an Underground Muon Detector [71] in the current SD 750 array that will be used for the verification and fine-tuning of the methods used to extract muon information from the SSD and WCD measurements. Furthermore, we are testing an extension of the operational mode of the FD into periods with a higher night sky background to increase its current duty cycle by 50%.

At this conference we presented the first results from the AugerPrime Engineering Array [70]

15

consisting of 12 AugerPrime detector stations that have been in operation since 2016. With this setup we have verified the basic functionality of the detector design, the linearity of the scintillator signal, the calibration procedures and operational stability. The physics potential of the upgraded stations is demonstrated by the first measurements of the lateral distribution of signals with the WCDs and SSDs. The construction of AugerPrime is expected to be finished by 2019 and it will take data until 2025. In this period, the number of events collected will be comparable with the statistics recorded up to now with the existing Observatory, but with the advantage of a mass estimate for each event and thus additional information to elucidate the origin of cosmic rays at ultra-high energies.

References

[1] All contributions can be found within one volume at [2]. Due to the page limitation only selected results are presented here and we refer the reader to [72–80] for further interesting results from the Pierre Auger Observatory presented at this conference.

[2] A. Aab *et al.* [Pierre Auger Coll.], [arXiv:1708.06592].

[3] A. Aab *et al.* [Pierre Auger Coll.], NIMA **798** (2015) 172,

[4] E.M. Holt [Pierre Auger Coll.], PoS ICRC17 492.

[5] F. Fenu [Pierre Auger Coll.], PoS ICRC17 486.

[6] J. Hersil *et al.*, PRL **6**, 22 (1961).

[7] A. Aab *et al.* [Pierre Auger Coll.], JCAP **1408** (2014) 019.

[8] M. Ave *et al.* [AIRFLY Coll.], APP **42** (2013) 90.

[9] J. T. Brack *et al.*, JINST **8** (2013) P05014.

[10] P. Abreu *et al.* [Pierre Auger Coll.], JINST **8** (2013) P04009.

[11] M. Malacari [Pierre Auger Coll.], PoS ICRC17 398.

[12] A. Aab *et al.* [Pierre Auger Coll.], APP **95** (2017) 44.

[13] V. Verzi for the Pierre Auger Coll., Proc. 33th ICRC 2013

[14] R. Krause [Pierre Auger Coll.], PoS ICRC17 528.

[15] A. Aab *et al.* [Pierre Auger Coll.], PRL **116** (2016) 241101.

[16] V. Berezinsky, A.Z. Gazizov, S.I. Grigorieva, PRD **74** (2006) 043005.

[17] J. Bellido [Pierre Auger Coll.], PoS ICRC17 490.

[18] A. Aab *et al.* [Pierre Auger Coll.], PRD **90** (2014) 122005.

[19] A. Aab *et al.* [Pierre Auger Coll.], PRD **90** (2014) 012012; Erratum-ibid: **92** (2015) 019903.

[20] A. Aab *et al.* [Pierre Auger Coll.], PRD **91** (2015) 032003.

[21] A. Aab *et al.* [Pierre Auger Coll.], PRL **117** (2016) 192001.

[22] A. A. Watson, J. G. Wilson, J. Phys. A **7** (1974) 1199.

[23] P. Sanchez-Lucas [Pierre Auger Coll.], PoS ICRC17 495.

[24] S. Ostapchenko, PRD **83** (2011) 014018.

[25] T. Pierog *et al.* PRC **92** (2015) 034906.

[26] F. Riehn *et al.* PoS ICRC **2015** (2016) 558.

[27] P. Abreu *et al.* [Pierre Auger Coll.], JCAP **1302** (2013) 026.

[28] A. Aab *et al.* [Pierre Auger Coll.], PRD **90** (2014) 122006.

[29] S. Buitink *et al.* [LOFAR Coll.], Nature **531** (2016) 70.

[30] W. D. Apel *et al.* [KASCADE Grande Coll.], PRL **107** (2011) 171104.

[31] W. D. Apel *et al.* [KASCADE Grande Coll.], PRD **87** (2013) 081101.

[32] A. Aab *et al.* [Pierre Auger Coll.], PLB **762** (2016) 288.

[33] A. Aab *et al.* [Pierre Auger Coll.], JCAP **1704** (2017) 038.

[34] D. Wittkowski [Pierre Auger Coll.], PoS ICRC17 563.

[35] K. Dolag *et al.*, JCAP **0501** (2005) 9.

[36] R. Alves Batista *et al.*, JCAP **1605** (2016) 038.

[37] M. Unger, G.R. Farrar, L.A. Anchordoqui, PRD **92** (2015) 123001.

[38] N. Globus, D. Allard, E. Parizot, PRD **92** (2015) 021302.

[39] S. Mollerach, E. Roulet, JCAP **1310** (2013) 013.

[40] I. Valiño [Pierre Auger Coll.], PoS ICRC (2015) 271.

[41] M. Niechciol [Pierre Auger Coll.], PoS ICRC17 517.

[42] E. Zas [Pierre Auger Coll.], PoS ICRC17 972.

[43] A. Aab *et al.* [Pierre Auger Coll.], ApJ **837** (2017) L25.

[44] P. Abreu *et al.* [Pierre Auger Coll.], ApJ **755** (2012) L4.

[45] B. P. Abbott *et al.* [LIGO and Virgo Coll.], PRL **116** (2016) 61102 and 241103.

[46] A. Aab *et al.* [Pierre Auger Coll.], PRD **94** (2016) 122007.

[47] P. Abreu *et al.* [Pierre Auger Coll.], PRL **109** (2012) 62002.

[48] A. Aab *et al.* [Pierre Auger Coll.], PRD **93** (2016) 72006.

[49] M. Mallamaci [Pierre Auger Coll.], PoS ICRC17 509.

[50] T. Pierog, PoS ICRC17 1100.

[51] S. Ostapchenko, M. Bleicher, PRD 93 (2016) 051501.

[52] O. Taborda [Pierre Auger Coll.], PoS ICRC17 523.

[53] A. Aab *et al.* [Pierre Auger Coll.], Science **357** (2017) 1266

[54] A. Aab *et al.* [Pierre Auger Coll.], ApJ **802** (2015) 111.

[55] M. Kachelriess, P. D. Serpico, PLB **640** (2006) 225.

[56] J. P. Huchra *et al.*, ApJS **199** (2012) 26.

[57] P. Erdogdu *et al.*, MNRAS **368** (2006) 1515.

[58] R. Jansson, G. R. Farrar, ApJ **757** (2012) 14.

[59] U. Giaccari [Pierre Auger Coll.], PoS ICRC17 483.

[60] A. Aab *et al.* [Pierre Auger Coll.], ApJ **804** (2015) 15.

[61] W.H. Baumgartner *et al.*, ApJS **207** (2013) 19.

[62] M. Ackermann *et al.* [Fermi-LAT Coll.], ApJ **222** (2016) 5.

[63] Y. Gao and P.M. Solomon, ApJS **152** (2004) 63.

[64] M. Ackermann *et al.* [Fermi-LAT Coll.], ApJ **755** (2012) 164.

[65] A. Aab *et al.* [Pierre Auger Coll.], [arXiv:1604.03637].

[66] D. Martello [Pierre Auger Coll.], PoS ICRC17 383.

[67] T. Suomijärvi [Pierre Auger Coll.], PoS ICRC17 450.

[68] A. Castellina [Pierre Auger Coll.], PoS ICRC17 397.

[69] R. Smida [Pierre Auger Coll.], PoS ICRC17 390.

[70] Z. Zong [Pierre Auger Coll.], PoS ICRC17 449.

[71] M.J. Figueira [Pierre Auger Coll.], PoS ICRC17 396.

[72] R. Colalillo [Pierre Auger Coll.], PoS ICRC17 314.

[73] A. Bridgeman [Pierre Auger Coll.], PoS ICRC17 323.

[74] A. Coleman [Pierre Auger Coll.], PoS ICRC17 326.

[75] D. Schmidt [Pierre Auger Coll.], PoS ICRC17 353.

[76] J. Blazek [Pierre Auger Coll.], PoS ICRC17 362.

[77] R. Gaior [Pierre Auger Coll.], PoS ICRC17 372.

[78] C. Timmermans [Pierre Auger Coll.], PoS ICRC17 392.

[79] S. Quinn [Pierre Auger Coll.], PoS ICRC17 395.

[80] D. Boncioli [Pierre Auger Coll.], PoS ICRC17 561.